IN-SITU **MINERALOGICAL AND GEOCHEMICAL ANALYSIS ON MERCURY WITH X-RAY DIFFRACTION AND X-RAY FLUORESCENCE.** D. F. Blake[1], E. B. Rampe[2], P. Sarrazin[3], T. F. Bristow[1], F. McCubbin[2] and K. Zacny[5]. [1]NASA Ames Research Center (david.blake@nasa.gov); [2]NASA Johnson Space Center; [3]eXaminArt, LLC and [4]Honeybee Robotics.

Introduction: Mercury is a geochemical end-member among the terrestrial planets, and as such, an *in-situ* surface investigation of its mineralogy and chemistry will greatly aid our understanding of planet formation and planetary evolution. Mercury is the most chemically reduced of the terrestrial planets, diverse in terms of surface compositions, and volatile rich [1 and refs. therein]. Upcoming orbital observations by BepiColombo will reveal its surface composition and other features in much greater detail [2]. However, the Mercurian surface lacks diagnostic spectral absorption features in the UV-VIS region, so the mineralogy of Mercury has only been inferred through normative calculations based on surface compositions [3-5].

X-ray diffraction (XRD) and X-ray fluorescence (XRF) analyses provide the most diagnostic and comprehensive mineralogical and geochemical characterization of rocks and soils by any spacecraft-capable technique, improved upon only by sample return and analyses in terrestrial laboratories [6]. XRD paired with quantitative XRF analyses of surface regolith on Mercury will yield:

- Identification of all minerals present >1 wt. %.
- Quantification of all minerals >3 wt. %, including their structure states and cation occupancies.
- Bulk geochemistry of all major, minor and trace elements.
- Abundance of all major elements present in each mineral (H and above).
- Valence state of all elements, including speciation of multi-valent species, such as Fe.
- Abundance and composition of X-ray amorphous components if present.

XRD/XRF Analysis on Mercury: The first X-ray diffractometer flown in space is the CheMin instrument on the Mars Science Laboratory *Curiosity* rover [7]. Improvements in X-ray technology coupled with lessons learned during a decade of CheMin operations on Mars by our team have guided the design of next generation XRD/XRF instruments intended for future deployment on Mars [8], the moon [9], Venus [10] and Mercury. Fig. 1 shows our design for a Mercury XRD/XRF based on the Venus instrument [10].

XRD geometry and XRD sample cell description: The collimated X-ray beam from the source is directed through a thin layer (~175 μm) of <150 μm grain size Mercury regolith confined between two 8 mm-diameter, 7 μm thick Kapton™ windows in the XRD sample cell (e.g., cell 1A in Fig. 1). The sample cell is shaken causing the loose powder to flow in a convection motion

through the beam. The 2-D pattern is summed circumferentially around the central non-diffracted beam to yield a conventional 1-D XRD pattern (Fig 2).

The instrument will employ Hybrid Pixel Detectors (HPDs) in place of the single CCD used in MSL-CheMin. HPDs are radiation hard and do not require cooling. An array of 4 HPDs increases the resolution of the instrument from 0.3° to 0.2° 2θ, sufficient to identify and quantify 3-pyroxene systems.
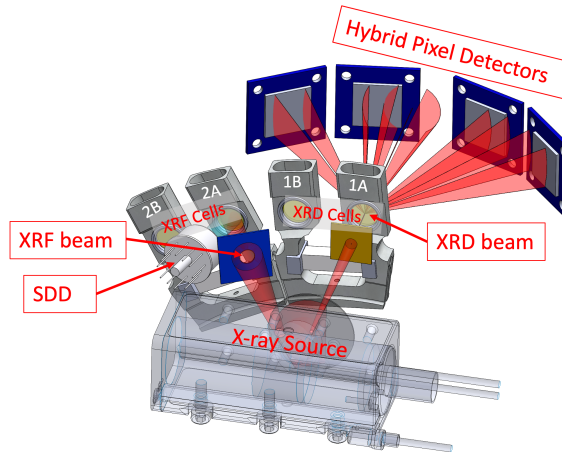

Fig. 1: Geometry of the Mercury XRD/XRF instrument. A single X-ray source emits two separate beams, the first optimized for XRD and the second optimized for XRF.

Fig. 2 shows an XRD pattern of Apollo 14 regolith sample 14149,26 collected in a 1 hour acquisition with a Terra™ XRD [11] (virtually identical XRD geometry to the Mercury XRD/XRF), and quantified using both Rietveld refinement [12] and whole pattern fitting [13]. The resulting analysis (from Rietveld refinement) is shown in Table 1.
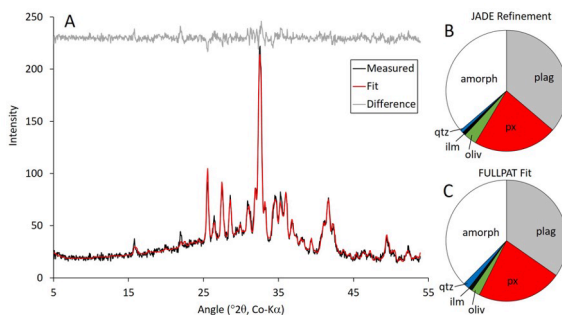

Fig. 2: One hour Terra XRD pattern of <150 μm grainsize separate of Apollo 14 regolith sample 14149,26. Inset pie diagrams show proportions of crystalline and amorphous components determined using Rietveld refinement and FULLPAT whole pattern fitting.

XRD performance of the Mercury XRD/XRF: XRD patterns can be refined using the Rietveld method [12] to obtain a wealth of crystal structural, compositional and valence data on individual mineral phases in a complex mixture [14], in addition to quantifying their abundances. Rietveld and full-pattern fitting methods such as FULLPAT [13] can be used to quantify the amount of X-ray amorphous material.

Table 1. Mineral Abundances and Compositions in Apollo 14 Regolith 14149,26

Mineral	Abundance[1]	Composition[2]
Plagioclase Feldspar	33.6 (0.8)	$Ca_{0.94(4)}Na_{0.06}Al_{1.94}Si_{2.06}O_8$
Augite	7.1 (0.6)	$Mg_{0.54(23)}Ca_{0.63(11)}Fe_{0.83(25)}Si_2O_6$
Orthopyroxene	8.5 (0.7)	$Mg_{1.27(6)}Fe_{0.61(6)}Ca_{0.12(2)}Si_2O_6$
Pigeonite	7.3 (0.7)	$Mg_{1.26(20)}Fe_{0.53(21)}Ca_{0.21(7)}Si_2O_6$
Olivine	3.5 (0.4)	$Mg_{1.46(10)}Fe_{0.54}SiO_4$
Quartz	0.9 (0.1)	SiO_2
Ilmenite	1.0 (0.2)	$FeTiO_3$
X-ray Amorphous	38.0 (6.0)	in combination with XRF data[3]
Total	99.7	

[1]Values in parentheses are 1σ errors. [2]Calculated from mineral unit-cell parameters [14] refined using MDI-JADE[TM]. [3]The composition of the X-ray amorphous component can be determined by subtracting the composition of the crystalline component (derived from unit cell parameters) from the bulk XRF composition.

XRF geometry and sample cell description: A divergent X-ray beam from the source fluoresces the active volume of the XRF sample cell (e.g., cell 2A in Fig. 1) which is 8 mm in diameter and 3 mm thick. The front window of the cell is made of an 8 mm-diameter, 4 μm-thick beryllium foil and the back window is made of an 8 mm-diameter Pt disc that is sufficiently thick to block X-ray transmission. XRF data are collected with a silicon drift detector (SDD) placed in reflection geometry (Fig. 1).

Predicted XRF performance of the Mercury XRD/XRF: Fundamental Parameters calculations [15] and Monte Carlo methods [16] were used to model the XRF performance of the instrument. These calculations simulate K, L, and M lines using source-sample-detector geometry of the instrument, sample absorption and fluorescence, SDD parameters and the X-ray tube spectrum [17]. Table 2 shows the calculated quantification and detection limits for select major, minor and trace elements in a basalt matrix for a 50 hour integration. Given the 0.3 year lifetime of the proposed Mercury Lander [18] longer integration times are possible to further improve mineralogical and elemental detection limits.

An instrument such as shown in Fig. 1 can analyze a single sample delivered by PlanetVac [19] with redundancy. Sample capacity can be increased to 2, 4 or more samples with increased complexity in sample delivery systems such as a drill-equipped PlanetVac.

The Advantage of Hybrid Pixel Detectors for XRD: HPDs do not require cooling, are radiation-hard and can operate under high flux conditions (Fig 3). These detectors will replace CCDs in all future XRD instruments developed by our group. We anticipate that the new detectors will allow for 3-5 times more X-ray flux, resulting in decreased analysis times and improved XRF performance, along with reduced power requirements.

Table 2, Quantification and Detection Limits in Basaltic or Rhyolitic Matrices Using XRF[1,2]

Major Elements			Zr, Selected REE and Th		
Element	Quant. Limit (PPM)	Det. Limit (PPM)	Element	Quant. Limit (PPM)	Det. Limit (PPM)
Na	84	26	Zr	2	1
Mg	34	11	La	2	1
Al	17	5	Ce	2	1
Si	13	4	Nd	1	1
P	11	4	Sm	1	1
S	4	2	Eu	8	3
Cl	3	1	Gd	6	2
K-Fe	1	1	Dy	17	6
			Er	6	2
			Yb	4	2
			Lu	4	1
			Th	3	1

[1] based on 50 hours of analysis.
[2] These are "best case" values that do not take into account peak interferences. "Real world" detection and quantification limits will commonly be higher, depending on matrix composition.
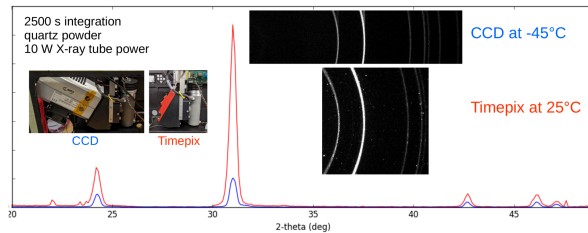

Fig 3: Comparison of XRD patterns of quartz powder, obtained with a CCD under single photon counting conditions and cooled to -45° C (blue) vs. a Timepix Hybrid Pixel Detector operated at room temperature (red).

References: [1] Armytage, et al., (2018), https://www.researchgate.net/publication/329504378. [2] Benkhoff et al., (2010), 10.1016/j.pss.2009.09.020. [3]. Vander Kaaden, et al., (2017), *Icarus* **285**, 155-168. [4] McCubbin et al., (2017), *J.G.R. Planets* **122**, 2053-2076. [5] Namur and Charlier, (2017), *Nature Geosci.* **10**, 9-13. [6] Velbel (2018), *Am. Min.*, **103**, 837-838. [7] Blake et al. (2012) *Space Sci. Rev.,* **170***, 341-478, 10.1007/s11214-012-9905-1. [8] Rampe et al. (2023), *this conference*. [9] Blake et al., (2022), *LPSC* **53**, Abstr #1612. [10] Blake, et al., (2023), *this conference*. [11] Sarrazin et al. (2008), *LPSC* **39**, #2421. [12] Bish, D.L & Post, J. E. (1993) *Am. Min.* **78**, 932–942. [13] Chipera & Bish (2002), *J. App. Cryst.*, **35**, 744-749. [14] Morrison et al., (2018) *Am. Min,.* 10.2138/am-2018-6123. [15] Solé´ et al, 2007) *Spectrochim. Acta Part B,* **62**, 63-68. [16] Schoonjans et al. (2012) *Spectrachim. Acta Part B, 70*, 10-23. [17] Ebel et al., (1999) *X-ray Spectrometry, 28*, 255-266. [18] Planetary Decadal Survey, p. C-11. [19] Zacny et al. (2014), *IEEE Aerospace Conference*, 3-7 March, Big Sky MT.